Insights From Closed-Form Expressions for Injection- and Production-Induced Stresses in Displaced Faults

Jansen, J. D.; Singhal, P.; Vossepoel, F. C.

DOI
10.1029/2019JB017932

Publication date
2019

Document Version
Final published version

Published in
Journal of Geophysical Research: Solid Earth

Citation (APA)
Jansen, J. D., Singhal, P., & Vossepoel, F. C. (2019). Insights From Closed-Form Expressions for Injection- and Production-Induced Stresses in Displaced Faults. *Journal of Geophysical Research: Solid Earth*, *124*(7), 7193-7212. https://doi.org/10.1029/2019JB017932

JGR Solid Earth

RESEARCH ARTICLE
10.1029/2019JB017932

Key Points:
- Closed-form expressions exist for fluid-induced elastic stresses in displaced vertical and inclined (normal or reverse) faults
- Slip in a reservoir with displaced faults will already occur for small amounts of injection or production
- Injection always causes slip in the over/underburden; for production, slip may remain in the reservoir

Supporting Information:
- Supporting Information S1

Correspondence to:
J. D. Jansen,
j.d.jansen@tudelft.nl

Citation:
Jansen, J. D., Singhal, P., & Vossepoel, F. (2019). Insights from closed-form expressions for injection- and production-induced stresses in displaced faults. *Journal of Geophysical Research: Solid Earth*, *124*, 7193–7212. https://doi.org/10.1029/2019JB017932

Received 27 APR 2019
Accepted 20 JUN 2019
Accepted article online 2 JUL 2019
Published online 31 JUL 2019

Insights From Closed-Form Expressions for Injection- and Production-Induced Stresses in Displaced Faults

J. D. Jansen[1], P. Singhal[1], and F. C. Vossepoel[1]

[1] Department of Geoscience and Engineering, Delft University of Technology, Delft, Netherlands

Abstract We consider fluid-induced seismicity and present closed-form expressions for the elastic displacements, strains, and stresses resulting from injection into or production from a reservoir with displaced faults. We apply classic inclusion theory to two-dimensional finite-width and infinite-width reservoir models. First, we simplify the fault model to the bare minimum while still maintaining its essential features: a vertical fault in a homogeneous reservoir of infinite width in an infinite domain. We confirm and sharpen findings from earlier numerical studies and furthermore conclude that the development of infinitely large elastic shear stresses in a displaced fault, at the internal and external reservoir/fault corners, implies that even small amounts of injection or production will result in some amount of slip or other nonelastic deformation. Another finding is that there is a marked difference between the shear stress patterns resulting from injection and production in a reservoir with a displaced fault. In both situations two slip patches emerge but at the start of injection some amount of slip occurs immediately in the overburden and underburden, whereas during production the slip may remain inside the reservoir region. Next we derive similar but more complicated expressions for displaced inclined (normal or reverse) faults and conclude that our findings for vertical faults also apply to inclined faults.

Plain Language Summary Injection of waste water or CO_2 in the deep subsurface, or production of natural gas from subsurface reservoirs, may produce earthquakes. Earlier studies have shown that these are especially likely to occur when the reservoir contains faults that have undergone earlier movements ("displaced faults"). We derive mathematical expressions that allow for an improved understanding of the stresses in these faults compared to earlier computer studies. We conclude, among other findings, that there is an essential difference between injection and production: for injection the fault movement is much more likely to propagate outside the reservoir than for production. Our theoretical insights do not have direct quantitative predictive value but are relevant for the interpretation of experimental and computer studies. They may also help to drastically speed up computer studies, for example, for hazard and risk assessments of injection into or production from deep reservoirs.

1. Introduction

We consider the incremental displacements, strains, and stresses inside and just outside subsurface reservoirs as a result of anthropogenic injection or production of fluids. More specifically, we consider situations where these quantities result from unequal deformations across faults ("differential compaction") and in particular across faults with a nonzero throw ("displaced faults"). Such fluid-induced stress changes are a likely cause for seismicity during production or reinjection (storage) operations in natural gas fields in the Netherlands (Nagelhout & Roest, 1997; Orlic et al., 2013; Roest & Kuilman, 1994) and in particular the huge Groningen field (Bourne & Oates, 2017; Buijze et al., 2017, 2019; Lele et al., 2016; Mulders, 2003; Orlic & Wassing, 2013; Thibault et al., 2018; Van den Bogert, 2015; Van Wees et al., 2017, 2018; Zbinden et al., 2017) and fields in Northern Germany that are located in a similar geological setting (Haug et al., 2018). The potential for induced seismicity due to reactivation of displaced faults has also been assessed for subsurface CO_2 storage in, for example, Cappa and Rutqvist (2011) and Rutqvist et al. (2016).

All of the above-mentioned studies employed numerical models to describe the effects of faulting on induced seismicity to various levels of detail and complexity. In the present paper we use analytical methods and consider a fault model that has been stripped to the bare minimum while still maintaining the essential features of a displaced fault. We aim to confirm numerical findings and gain further insight in the mechanisms that govern induced seismicity. Therefore, we will analytically compute the stresses in a faulted reservoir resulting from injection or production and, in particular, the normal and shear stresses in the fault plane such that we can determine the locations where slip will occur.

2. Inclusion Theory and the Nucleus of Strain Concept

Linear elastic displacements, strains, and stresses inside and outside a reservoir undergoing injection or production can be determined with the "theory of inclusions" as introduced by Eshelby (1957). Inclusion theory is closely related to the "nucleus of strain" concept (Love, 1927) as discussed in detail by Rudnicki (2002); see also Mura (1987) and section S1 of the supporting information for this paper. Inclusion theory and the nucleus of strain concept have been reported in the geophysics literature for various purposes: to compute stresses around boreholes (Geertsma, 1966), to estimate production-induced subsidence above hydrocarbon reservoirs (Gambolati, 1972; Geertsma, 1973; Segall, 1992; Walsh, 2002), and to compute stress fields around producing reservoirs in order to establish the risk on reactivation of nearby (nondisplaced) faults (Segall, 1985, 1989, 1992; Segall et al., 1994). The latter four papers, by Segall and coworkers, address stresses and their potential effect on fault reactivation outside the reservoir. A follow-up paper (Segall & Fitzgerald, 1998) also considers the stresses inside the reservoir, based on the classic results in Eshelby (1957) for an elliptic inclusion. Further work along those lines was done by Rudnicki (1999), who considered a reservoir with elastic properties that differed from those of the surroundings and by Soltanzadeh and Hawkes (2008, 2009) who elaborated on the effects of reservoir geometry and orientation. A detailed analysis, based on inclusion theory, of the radial and vertical deformations around a vertical well under transient conditions was presented by Marck et al. (2015).

3. Displacements, Strains, and Stresses

The three-dimensional (3-D) equations for poroelasticity were first derived by Biot (1941) and have since been reproduced in various forms; see, for example, Wang (2000) or Cheng (2016) for overviews. We consider an application of the theory in the form of 2-D expressions for incremental displacements $u_i(x, y)$, $i \in \{x, y\}$ under plane-strain conditions resulting from the injection or production of fluids in a reservoir (i.e., a porous and permeable medium) which forms an inclusion Ω inside an otherwise nonpermeable infinite domain with the same elastic properties as the inclusion

$$u_i(x, y) = \iint_{\Omega} D(\zeta, \xi)\, g_i(x, y, \zeta, \xi)\, \mathrm{d}\Omega. \tag{1}$$

Here x and y are the usual 2-D Cartesian coordinates, while ζ and ξ are x and y coordinate values inside Ω. The symbol g_i indicates Green's functions (with SI unit meter inverse) which are given in Segall (1985) and which have been reproduced, together with a brief derivation, in section S1 of the supporting information. (Note that all variables and their SI units have been listed in section S5 of the supporting information). These Green's functions are solutions of the equilibrium equations from the theory of elasticity for the displacements in a solid caused by a "center of dilation," also known as a center of dilatation. Such a center is a particular form of a "nucleus of strain," consisting of two orthogonal pairs of opposing point forces of equal strength (in 2-D) which, in our case, represent the injection or production of fluid from the reservoir (Dougall, 1897; Huynen & Detournay, 2014; Love, 1927; Rudnicki, 2002; Wang, 2000). The integral in equation (1) ensures linear superposition to represent the effect of nuclei of strain distributed over the entire reservoir domain Ω.

The dimensionless function $D(\zeta, \xi)$ is defined as

$$D(\zeta, \xi) = \frac{(1 - 2\nu)\alpha p(\zeta, \xi)}{2\pi(1 - \nu)G} = \frac{(1 + \nu)\alpha p(\zeta, \xi)}{3\pi(1 - \nu)K}, \tag{2}$$

where p is the incremental pore pressure in the reservoir (positive for injection and negative for production) which may be a function of location (ζ, ξ). The parameter α is Biot's coefficient, K and ν are the bulk modulus and Poisson's ratio under drained conditions (i.e., only reflecting the stiffness of the grains), and G is the shear modulus. For definitions and physical interpretations of these parameters, see, for example, Wang (2000), Verruijt (2016), or Cheng (2016). Alternatively, $D(\zeta, \xi)$ can be expressed as, for example,

$$D(\zeta, \xi) = \frac{B(1 + \nu_u)v_f(\zeta, \xi)}{3\pi(1 - \nu_u)} = \frac{B(1 + \nu_u)m_f(\zeta, \xi)}{3\pi\rho^0(1 - \nu_u)}, \tag{3}$$

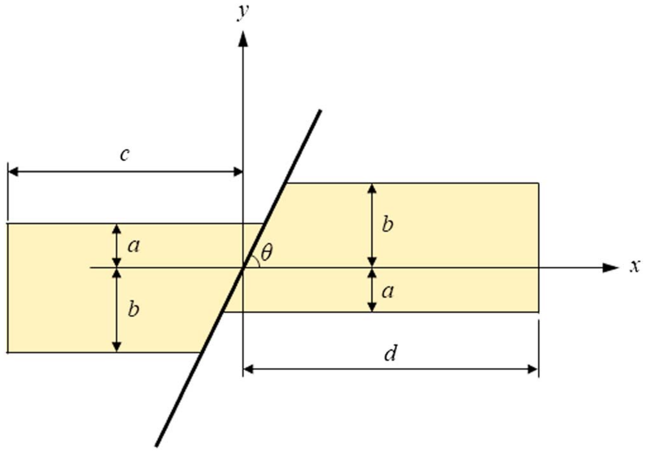

Figure 1. Reservoir with a displaced normal fault.

where B is Skempton's pore pressure coefficient, ν_u is Poisson's coefficient under undrained conditions, ρ^0 is initial fluid density, v_f is the incremental fluid volume per unit reservoir volume and m_f is the incremental fluid mass per unit reservoir volume. The latter variety of equation (3), expressed in terms of m_f, is the form used in Segall, (1985, 1989); the formulation in equation (2) in terms of p is used in Soltanzadeh and Hawkes (2008, 2009) and also in the remainder of this paper. We refer to Rudnicki (2002) for a detailed discussion of these formulations.

Expressions similar to equation (1) can be obtained for the incremental stresses $\sigma_{ij}, i \in \{x, y\}, j \in \{x, y\}$ inside and outside the reservoir in response to injection or production

$$\sigma_{ij}(x, y) = \iint_{\Omega} C(\zeta, \xi)\, g_{ij}(x, y, \zeta, \xi)\, \mathrm{d}\Omega - C(x, y)\, 2\pi\, \delta_{\Omega}, \tag{4}$$

where $C = GD$ (with SI unit Newton per meter squared) and $g_{ij}(x, y, \zeta, \xi)$ are Green's functions for the incremental stresses which, like the ones for incremental displacements used in equation (1), are given in Segall (1985) and have been reproduced in section S1 of the supporting information. The symbol δ_Ω is a modified Kronecker delta defined as

$$\delta_{\Omega} = \begin{cases} 1 & \text{if } (x, y) \in \Omega \\ 0 & \text{if } (x, y) \notin \Omega \end{cases}, \tag{5}$$

which ensures that the term $C(x, y)2\pi$, representing "eigen stresses" σ^*_{ij} resulting from the injection or production of fluids, is only subtracted for points inside the reservoir; see section S1 of the supporting information. If we ignore transient effects, that is, if we assume pseudo steady-state pore pressure changes in the reservoir, the functions $C(x, y)$ and $D(x, y)$ become parameters C and D, respectively, and the integrals in equations (1) and (4) only have to be taken over the Green's functions.

Note that in equations (2) and (3), we employ the notation p, v_f, and m_f to indicate incremental quantities, that is, in addition to those before starting injection or production. In a similar fashion we use the variables u_i and σ_{ij} to indicate incremental displacements and incremental stresses. However, from now on we will simply refer to these quantities as "displacements" and "stresses" and avoid the use of the adjective "incremental" except in situations where the difference between initial and incremental quantities is important. Also, note that a 2-D description uses the concept of unit thickness (perpendicular to the paper plane, i.e., in the strike direction of the fault). Relevant quantities should therefore be interpreted as being defined per unit strike length with the corresponding dimensions and units. For example, shear forces in a fault are expressed in SI units Newton per meter rather than in Newton as they would in 3-D.

4. Faulted Reservoir

Consider a finite reservoir in an infinite domain, with height h and width w (after faulting); see Figure 1. The domain and the reservoir are both divided into two parts through the presence of a fault of infinite extent with dip θ and throw t and various other geometrical features as indicated in the figure from which it follows that

$$h = a + b, \tag{6}$$

$$w = c + d, \tag{7}$$

$$t = b - a. \tag{8}$$

We assume that flow from the reservoir to the surrounding area or vice versa is impossible. Moreover, we assume that the reservoir and the surroundings have identical, uniform elastic properties and that the fault is nonsealing but does not transmit pressure outside the reservoir. The latter assumption could be relaxed, and the effects of pressure propagation in the fault above and below the reservoir zone could also be addressed with inclusion theory. However, we have chosen not to do so, to simplify the analysis.

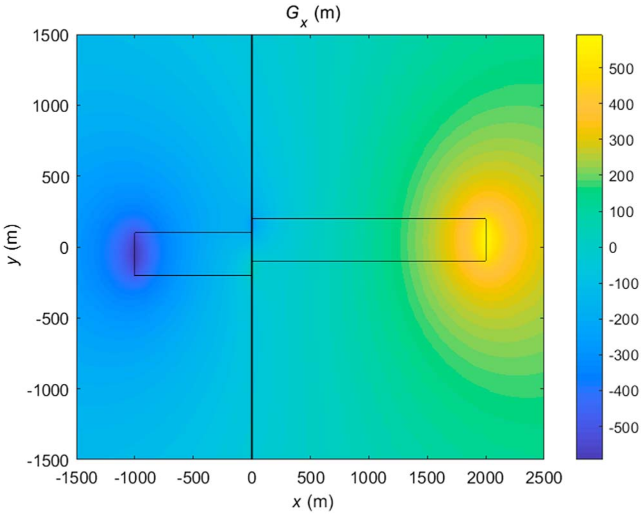

Figure 2. Scaled horizontal displacements $\frac{u_x}{D}$. The dimensionless scaling parameter D has magnitude 3.63×10^{-4} for the parameter values listed in Table 1.

5. Vertical Fault in a Finite Reservoir

As a first step, we further restrict our analysis to the case of a vertical fault (i.e., $\theta = \pi/2$), which we consider to be an acceptable approximation if the reservoir is located in a normal faulting regime where faults are typically steeply dipping. (Exact solutions for normal and reverse faults will be addressed in section 9). To compute the displacements u_i, we need to integrate Green's function g_i over the reservoir domains Ω_l and Ω_r to the left and the right of the fault

$$\begin{aligned} G_i(x,y) &= \iint_{\Omega_l} g_i(x,y,\zeta,\xi)\,\mathrm{d}\Omega + \iint_{\Omega_r} g_i(x,y,\zeta,\xi)\,\mathrm{d}\Omega \\ &= \int_{-c}^{0}\int_{-b}^{a} g_i(x,y,\zeta,\xi)\,\mathrm{d}\xi\mathrm{d}\zeta + \int_{0}^{d}\int_{-a}^{b} g_i(x,y,\zeta,\xi)\,\mathrm{d}\xi\mathrm{d}\zeta. \end{aligned} \tag{9}$$

The integrals can be evaluated in closed form, and the results for a general rectangular domain have been given in section S2 of the supporting information. Their values represent scaled horizontal and vertical

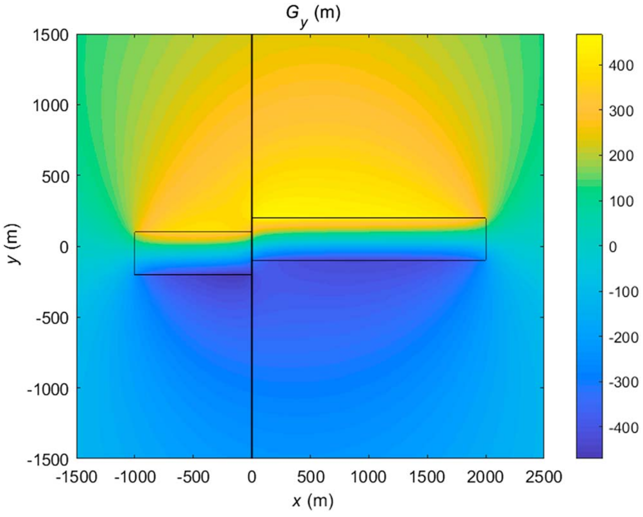

Figure 3. Scaled vertical displacements $\frac{u_y}{D}$. Scaling parameter D as in Figure 2.

Table 1
Reservoir Properties and Fault Geometry for Example 1

Symbol	Property	Value	SI units
a	See Figure 1	100	m
b	See Figure 1	200	m
c	See Figure 1	1,000 or ∞	m
d	See Figure 1	2,000 or ∞	m
G	Shear modulus	6,500	MPa
p	Incremental reservoir pressure	20	MPa
p^0	Initial reservoir pressure	35	MPa
α	Biot's coefficient	0.9	—
θ	Dip angle	$\pi/2$	rad
μ_{st}	Static friction coefficient	0.60	—
ν	Poisson's coefficient	0.15	—
σ_{xx}^0	Initial horizontal stress	−60	MPa
σ_{xy}^0	Initial shear stress	15	MPa

displacements according to

$$G_i(x, y) = \frac{u_i}{D}. \tag{10}$$

Note that D is a linear function of the incremental pressure p such that a change in sign of p, that is, a change from injection to production, also results in a sign change of u_i but not of G_i.

Figures 2 and 3 display the values for $G_x(x, y)$ and $G_y(x, y)$ (with SI unit meter) as computed with the expressions from section S2 of the supporting information for an isotropic reservoir with parameters given in Table 1. The parameter values have the same order of magnitude as those of the Groningen natural gas reservoir (NAM, 2016) except for the relatively high initial shear stress. This implies that the fault is initially near-critically stressed which is generally believed not to be the case in the Groningen field, as will be discussed in more detail below. We chose values for the initial horizontal stress σ_{xx}^0 and initial shear stress σ_{xy}^0 directly, instead of computing those from an initial vertical stress and a ratio of horizontal to vertical stresses, as is the usual approach, to allow for the specification of initial shear stress on the vertical fault. In section 9 we will address inclined faults and consider the usual situation in which the horizontal and vertical stresses are also the principal stresses, which is not the case in the present example. However, we note that neither the initial near-critically stressed state of the fault nor the unusually oriented principal stresses influence the main conclusions of our paper. The positive value of p as used in the definition of D corresponds to injection resulting in expansion of the reservoir.

Note that, because we consider an infinite domain, the upward displacements at the top of the reservoir are just as large as the downward displacements at the bottom. In an actual situation the vertical displacements will be nearly completely accommodated by an upward motion of the overburden. For a complete analysis of the displacement field one should therefore revert to the infinite half-space solution as detailed in Segall (1989). However, in the present paper we primarily address the stresses around the fault which depend on the relative displacements rather than the absolute ones. For a sufficiently deep reservoir (relative to the reservoir height) the free surface effects on the relative displacements are negligible and therefore the relatively simple infinite space solution is suitable for our purpose.

Numerical experiments based on the expressions from section S2 of the supporting information indicate that for an increasing reservoir width w, that is, for increasing values of c and d, the stress concentrations near the two vertical outer boundaries are decreasingly affecting the displacements near the fault, even though their values at the boundaries do increase. In the present paper we are primarily interested in the behavior of the reservoir and its surroundings in the vicinity of a displaced fault that is sufficiently away from the edges of the reservoir. Therefore, we will from now on use the limit of an infinitely wide reservoir. (For discussions about the behavior of a rectangular reservoir bounded by a fault at the edge, see, e.g., Orlic & Wassing, 2013 and Van Wees et al., 2014).

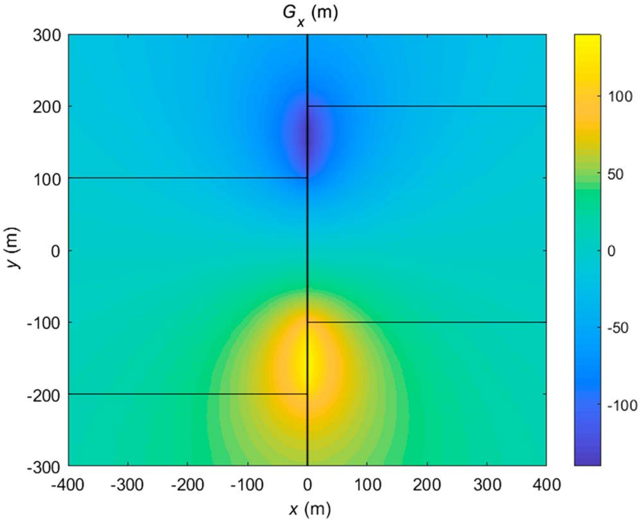

Figure 4. Scaled horizontal displacements $\frac{u_x}{D}$. Scaling parameter D as in Figure 2.

6. Vertical Fault in an Infinite Reservoir

6.1. Displacements

Closed-form expressions for the limit of an infinite reservoir, that is, for $c = d \to \infty$ while $-c < x < d$, are given in section S3 of the supporting information. The values of G_x and G_y corresponding to Example 1, but now with an infinite width, have been displayed in Figures 4 and 5 which are now only showing the area around the fault. Note the difference in scale (color bars) between Figures 2 and 4. It can be seen that horizontal displacements are concentrated in the areas where the reservoir rock juxtaposes the overburden and underburden, whereas the vertical displacements are relatively smoothly following the throw of the fault. Recall that we consider an elastic solution for the displacements. In reality inelastic deformations may occur in areas of high stresses (in the form of plasticity or fault slip) which will then modify the displacement patterns in Figures 2 to 5.

6.2. Stresses

We also derived closed-form expressions for the integrals G_{ij} which represent scaled (dimensionless) stresses according to

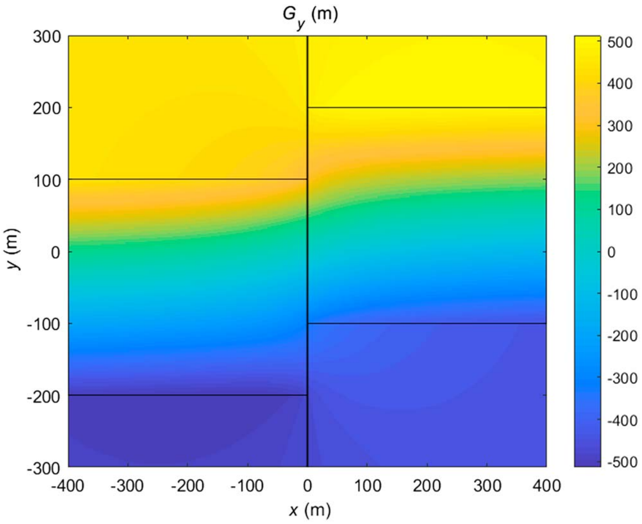

Figure 5. Scaled vertical displacements $\frac{u_y}{D}$. Scaling parameter D as in Figure 2.

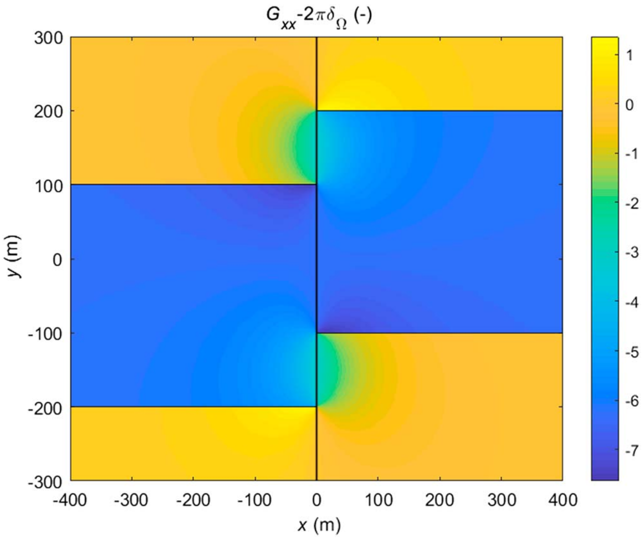

Figure 6. Dimensionless horizontal stresses $\frac{\sigma_{xx}}{C}$. The scaling parameter C has magnitude 2.36×10^6 N/m^2 for the parameter values listed in Table 1.

$$G_{ij}(x, y) - 2\pi\delta_\Omega = \frac{\sigma_{ij}}{C} \tag{11}$$

and which are sometimes referred to as “arching ratios” or “normalized stress path parameters”; see, for example, Mulders (2003), Soltanzadeh and Hawkes (2008), or Van Wees et al. (2017) who used similar definitions but with slightly different scale factors. Note that the sign of G_{ij} is independent of the sign of C, just as the sign of G_i was independent of the sign of D in equation (10). The full expressions for the integrals G_{xx}, G_{yy}, and G_{xy} over a rectangular domain are given in section S2 of the supporting information, while their approximations for an infinite reservoir are given in section S3. Figures 6, 7 and 8 display the scaled near-fault stresses corresponding to the parameters for Example 1 listed in Table 1 but now with $c = d = \infty$.

It can be seen from Figures 6 and 7 that the expansion of the reservoir results in compression (negative normal stresses) inside the reservoir and mostly very small tension (positive normal stresses) around it. The values of the horizontal tension stresses outside the reservoir are approaching zero because compressive stresses in the finite-height reservoir are compensated by tension stresses in the infinitely high and deep overburden and underburden. Note that the normal stresses perpendicular to the reservoir boundaries and the shear stresses are continuous, whereas the normal stresses parallel to the reservoir boundaries (which are sometimes referred to as “hoop stresses”) show a jump, a well-known feature of inclusion theory. The magnitude of the jump, in our scaled formulation, is equal to $2\pi C$ as can be verified with the aid of the color bars. Also note that the horizontal stresses have a magnitude of $-\pi C$ in those parts of the fault where the reservoir rock juxtaposes the overburden and underburden, while they have a magnitude of $-2\pi C$ in the part of the fault where reservoir juxtaposes reservoir. Figure 9 shows the (scaled) average of the two in-plane stresses σ_{xx} and σ_{yy} which is linearly related to total strain $\epsilon = \epsilon_{xx} + \epsilon_{yy}$. It can be seen that this average is zero outside the reservoir and has a constant value $-\pi C$ inside. This illustrates that there is no dilation (i.e., that $\epsilon = 0$) and only distortion outside the reservoir which is also a known effect for rectangular inclusions (Bhargava & Kapoor, 1966). We reiterate that, similar to the displacements in Figures 2 to 5, the stresses in Figures 6 to 9 are based on an elastic solution. Inelastic deformations in areas of high stresses may therefore modify the stress patterns. Finally, we note that although we restrict the analysis to a 2-D configuration, the underlying inclusion theory allows for the derivation of similar expressions in 3-D (Mura, 1987).

6.3. Expressions for the Fault Plane

If we only consider the values in the fault, that is, if we set $x = 0$, equations (C.1) and (C.2) for the integrals G_x and G_y given in section S3 of the supporting information can be reduced to

$$\begin{aligned} G_x(0, y) = {} & \ln\left[(y-a)^2\right] \times \frac{y-a}{4} - \ln\left[(y+b)^2\right] \times \frac{y+b}{4} \\ & + \ln\left[(y+a)^2\right] \times \frac{y+a}{4} - \ln\left[(y-b)^2\right] \times \frac{y-b}{4}, \end{aligned} \tag{12}$$

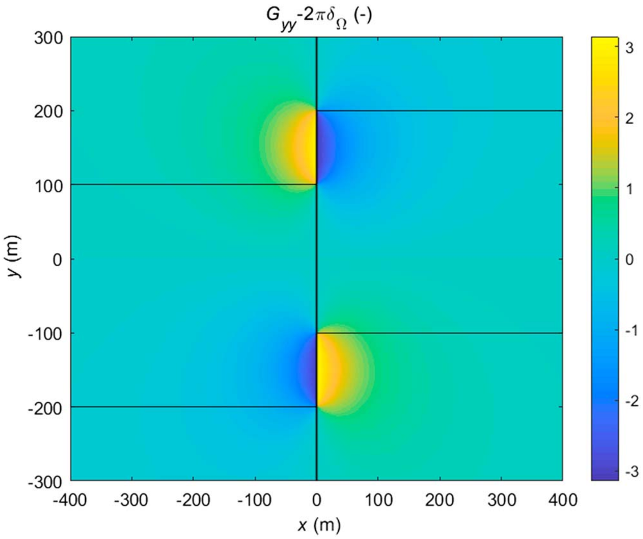

Figure 7. Dimensionless vertical stresses $\frac{\sigma_{yy}}{C}$. Scaling parameter C as in Figure 6.

$$G_y(0, y) = \frac{\pi}{4}\left(|y + a| - |y - a| - |y - b| + |y + b|\right). \tag{13}$$

Similarly, the values at $x = 0$ of the integrals G_{xx}, G_{yy}, and G_{xy} for an infinite reservoir can be derived from equations 43, 44, and 45 in section S3 of the supporting information as

$$\lim_{x\downarrow 0} G_{xx}(x, y) = \frac{\pi}{2}\left[\mathrm{sgn}(y + a) + \mathrm{sgn}(y - a) - \mathrm{sgn}(y - b) - \mathrm{sgn}(y + b)\right], \tag{14}$$

$$G_{yy}(0, y) = \frac{\pi}{2}\left[\mathrm{sgn}(y + a) - \mathrm{sgn}(y - a) - \mathrm{sgn}(y - b) + \mathrm{sgn}(y + b)\right], \tag{15}$$

$$G_{xy}(0, y) = \frac{1}{2}\ln\frac{(y - a)^2(y + a)^2}{(y - b)^2(y + b)^2}, \tag{16}$$

where

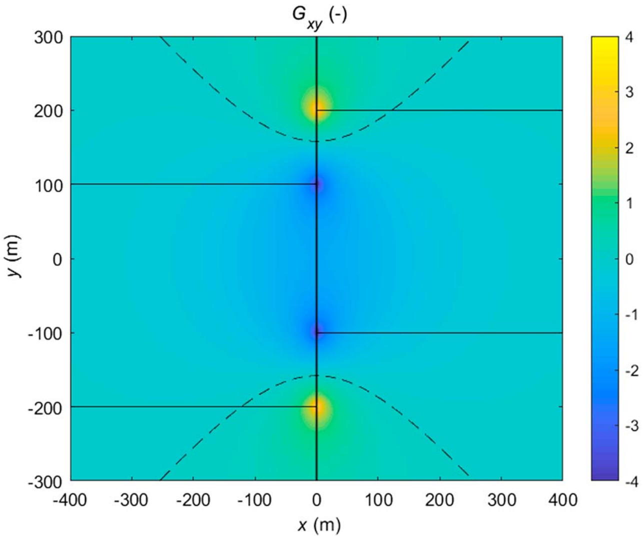

Figure 8. Dimensionless shear stresses $\frac{\sigma_{xy}}{C}$. Scaling parameter C as in Figure 6.

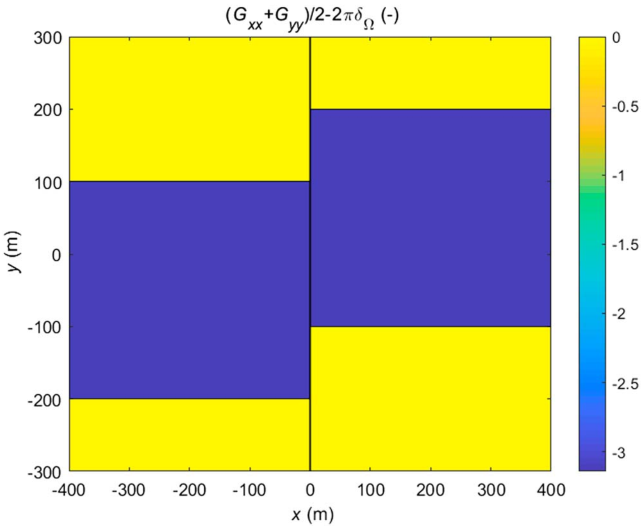

Figure 9. Dimensionless average in-plane stresses $\frac{(\sigma_{xx}+\sigma_{yy})}{2C}$. Scaling parameter C as in Figure 6.

$$\operatorname{sgn}(\cdot) = \begin{cases} 1 \text{ if } (\cdot) > 0 \\ 0 \text{ if } (\cdot) = 0 \\ -1 \text{ if } (\cdot) < 0 \end{cases} . \tag{17}$$

Note that for G_{xx} we consider a limit that is valid for values to the right of the fault. It can be seen from equation (16) that the shear stresses have singularities at $y = \pm a$ and $y = \pm b$ which implies that their values approach plus or minus infinity at those points. This is a well-known feature for the corners of rectangular inclusions (Goodier, 1937; Bhargava & Kapoor, 1966). In reality, small amounts of slip in the fault and nonelastic deformation of the reservoir rock in those regions with high shear stresses will flatten the peaks such that the stress values remain finite. Note that we restricted the scale in Figure 8 to the range $-4 \leq G_{xy} \leq 4$, such that the infinite shear stress values are suppressed. The dashed lines in Figure 8 indicate the boundaries between positive and negative shear stresses as given by equation (57) in the supporting information. It can also be seen from equation (16) above that for a zero throw fault, that is, when $a = b$, the shear stresses vanish.

7. Shear and Coulomb Stresses

7.1. Shear Stresses

To further analyze the nature of the shear stresses G_{xy}, we revert to equation (45) in the supporting information

$$G_{xy}(x, y) = \frac{1}{2} \ln \frac{\left[x^2 + (y-a)^2\right]\left[x^2 + (y+a)^2\right]}{\left[x^2 + (y-b)^2\right]\left[x^2 + (y+b)^2\right]}, \tag{18}$$

which reduces to equation (16) for $x = 0$. Values of G_{xy} for Example 1, for various fixed values of x, have been displayed in Figure 10. The figure illustrates that the shear stresses have their maximum value in the fault and drop to negligible values at horizontal distances from the fault equal to approximately the height of the reservoir. Note that, like before, we restricted the scale, in this case to the range $-8 \leq G_{xy} \leq 8$, such that the infinite shear stress values in the fault at $y = \pm 100$ m and $y = \pm 200$ m are suppressed.

The boundaries between positive and negative shear stresses for $x = 0$ follow from equation (57) in the supporting information as

$$y_0 = \pm\sqrt{\frac{a^2 + b^2}{2}} = \pm\sqrt{\frac{h^2 + t^2}{2}}, \tag{19}$$

which for Example 1 results in $y_0 = \pm 158$ m. It is clear from Figure 8 that there are four locations along the fault where shear stress concentrations occur, two with negative and two with positive values, symmet-

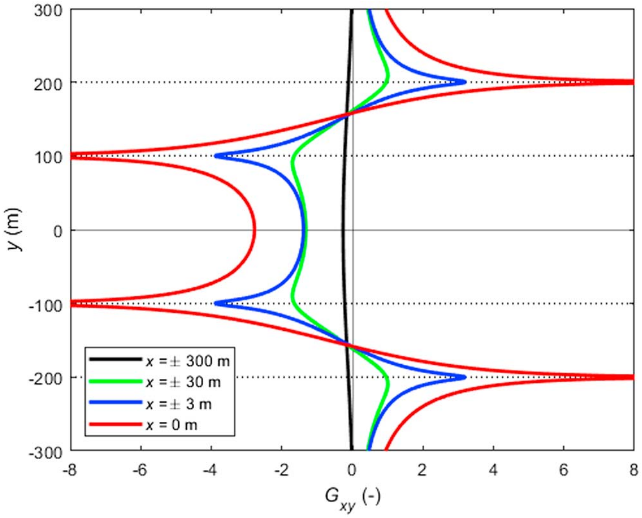

Figure 10. Dimensionless shear stresses $\frac{\sigma_{xy}}{C}$ for constant values of x. Scaling parameter C as in Figure 6.

rically oriented with respect to the x axis. Accordingly, the total shear force along the fault can be divided in four contributions, two with a negative and two with a positive magnitude. Section S4 of the supporting information gives closed-form expressions for these contributions and also demonstrates that the total shear force along the fault is equal to zero.

It follows from equations (11) and (18) that the elastic shear stress pattern, that is, the shape of the curves in Figure 10, only depends on the values of the geometric parameters a and b (or, alternatively, h and t) for an infinite reservoir. The scale factor C, and therefore the pressure p, just acts as a linear multiplier for the magnitude of the scale. Similar conclusions hold for the patterns of the horizontal and vertical stresses and for finite-width reservoirs in which case the relevant geometric parameters are a, b, c, and d (or h, t, c, and d). However, in reality the occurrence of fault slip will result in a redistribution of stresses such that an increasing or decreasing p does influence the stress patterns.

7.2. Coulomb Stresses

Slip-provoking conditions at the vertical fault plane occur when

$$0 < |\sigma^0_{xy} + \sigma_{xy}| + \mu_{\mathrm{st}}({\sigma'}^0_{xx} + {\sigma'}_{xx}), \tag{20}$$

where μ_{st} is the static friction coefficient and σ^0_{xy} and ${\sigma'}^0_{xx}$ are the initial shear stress and the initial effective horizontal stress, respectively (present before the start of fluid injection or production), while σ_{xy} and σ'_{xx} are their incremental counterparts. We did not include cohesion in the friction model, but this could be done without difficulty. The initial effective horizontal stress is related to the initial total horizontal stress σ^0_{xx} according to

$${\sigma'}^0_{xx} = \sigma^0_{xx} + \alpha p^0, \tag{21}$$

where p^0 is the initial pore pressure, while a similar expression holds for the incremental effective horizontal stress

$$\sigma'_{xx} = \sigma_{xx} + \alpha p. \tag{22}$$

(Recall that in our sign convention compressive normal stresses are negative whereas pore pressure is positive.) The right-hand side of equation (20) is known as the Coulomb stress which is a convenient concept if the faulting tendency is known, that is, if the initial shear stress σ^0_{xy} has a known sign and is large enough to avoid a sign reversal after addition of the incremental shear stress σ_{xy}. However, the presence of infinitely high incremental shear stresses of both positive and negative sign implies that slip will occur in both directions. We therefore rewrite equation (20) as

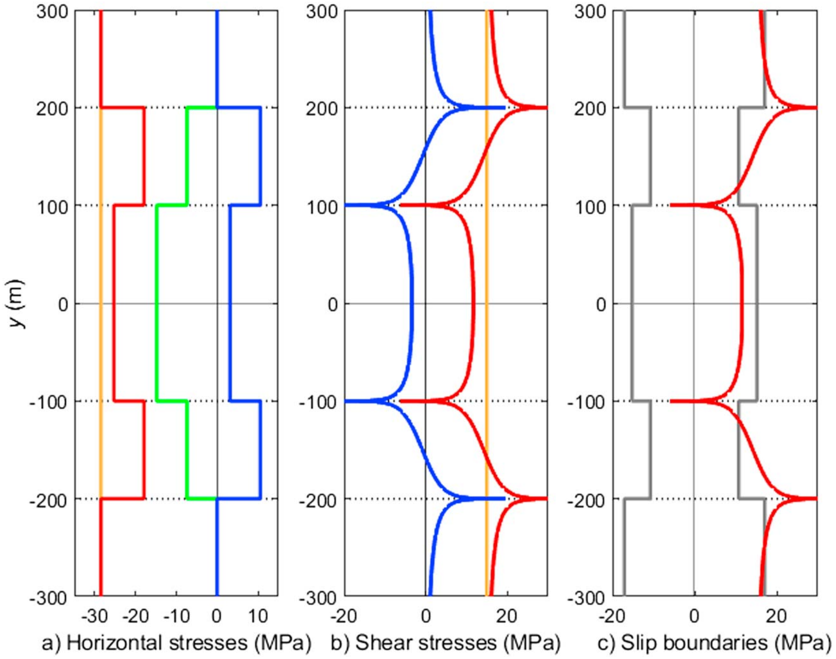

Figure 11. Stresses at the fault plane during injection ($p = 20$ MPa) for Example 1 with $c = d \rightarrow \infty$. (a) Horizontal (normal) stresses; orange: $\sigma_{xx}'^{0}$, green: σ_{xx}, blue:σ_{xx}', red: $\sigma_{xx}'^{0} + \sigma_{xx}'$. (b) Shear stresses; orange: σ_{xy}^{0}, blue: σ_{xy}, red: $\sigma_{xy}^{0} + \sigma_{xy}$. (c) Regions of slip; red: $\sigma_{xy}^{0} + \sigma_{xy}$ (shear stresses), gray: $\pm\mu_{\mathrm{st}}(\sigma_{xx}'^{0} + \sigma_{xx}'$; (slip thresholds); shear values to the left of the left threshold and to the right of the right threshold will result in fault slip.

$$\begin{aligned} \sigma_{xy}^{0} + \sigma_{xy} &> -\mu_{\mathrm{st}}(\sigma'^{0}_{xx} + \sigma'_{xx}) \text{ if } \sigma_{xy}^{0} + \sigma_{xy} > 0, \\ \sigma_{xy}^{0} + \sigma_{xy} &< \quad \mu_{\mathrm{st}}(\sigma'^{0}_{xx} + \sigma'_{xx}) \text{ if } \sigma_{xy}^{0} + \sigma_{xy} < 0. \end{aligned} \tag{23}$$

Thus, we start from a fault with a given offset and given initial elastic stresses. Next we add the incremental elastic stresses resulting from injection or production, and thereafter, we use the Coulomb friction model to determine at which locations of the fault additional slip will occur.

For an inclined fault in the coordinate system displayed in Figure 1, a positive shear stress corresponds to a normal faulting tendency which is in line with the depicted configuration where the right and left blocks are the footwall and the hanging wall, respectively. For a vertical fault the difference between normal and reverse faulting is not defined, and a positive shear stress just implies that the left block moves downward relative to the right block. To avoid complexities in the interpretation of sign changes, we will not use the dimensionless stresses G_{ij} but work with dimensional expressions directly. For the incremental stresses we can then write

$$\sigma'_{xx} = C\left(G_{xx} - 2\pi\,\delta_{\Omega}\right) + \alpha p\,\delta_{\Omega} = C\left[G_{xx} + 2\pi\left(\frac{1-\nu}{1-2\nu} - 1\right)\delta_{\Omega}\right], \tag{24}$$

$$\sigma_{xy} = CG_{xy}. \tag{25}$$

Simple expressions for G_{xx} and G_{xy}, valid for an infinitely wide reservoir, are given by equations (14) and (16), while expressions for a finite-width reservoir can be obtained from section S2 of the supporting information.

Figure 11 depicts the normal and shear stresses along the fault plane for Example 1 with an infinite reservoir. It can be seen in Figure 11a that although the total incremental stresses (green) are negative, that is, compressive, over the entire height of the reservoir, the effective incremental stresses (blue) are positive for this example. The combined initial (orange) and incremental (blue) effective stresses are indicated with a red line and are compressive. Figure 11b depicts the shear stresses. The orange line indicates the initial shear stresses, the blue line the incremental shear stresses, and the red line the combined (initial plus incremental) shear stresses. Figure 11c depicts the same combined shear stresses (red) in combination with two slip thresholds (gray). Shear stresses to the right of the right threshold result in "normal" slip such that the right block moves up and the left one down. Shear stresses to the left of the left threshold result in "reverse" slip.

In the initial situation, that is, before the start of injection or production, the magnitude of the initial shear stress, $\sigma_{xy}^0 = 15$ MPa, is below the magnitude of the right slip threshold, $\sigma_{\text{slip,st}} = \mu_{\text{st}}|\sigma_{xx} + \alpha p_0| = 0.60 \times |-60 + 0.9 \times 35| = 17.1$ MPa, where we used a static friction coefficient $\mu_{\text{st}} = 0.60$. However, the fault is near-critically stressed in the sense that even for a mild stress drop under dynamic conditions, for example, for a dynamic friction coefficient $\mu_{\text{dyn}} = 0.50$, we find that $\sigma_{\text{slip,dyn}} = \mu_{\text{dyn}}|\sigma_{xx} + \alpha p_0| = 14.25$ MPa such that the initial shear stress exceeds the slip threshold. In other words, the static shear capacity utilization (SCU) is $15/17.1 = 0.88$ but the dynamic SCU is $15/14.25 = 1.05$. Consequently, in this initial situation any initiation of slip may result in a runaway propagation of slip along the fault until reaching a heterogeneity or a change in stress state that stops the slip patch from growing further. We reiterate that this near-critical initial stress state is not an essential part of the theory in our paper, and the main conclusions therefore also hold for situations where the initial stresses are noncritical.

Qualitatively, the results for regular slip in Figure 11c are in agreement with those found in earlier numerical studies; see, for example, Figures 7a, 7c, 7e, and 8a in Van Wees et al. (2017), with the exception of one major difference: Van Wees et al. (2017) considered production rather than injection resulting in the occurrence of positive peak shear stresses at the internal corners of the reservoir and the fault (located at $y = \pm 100$ m in our example), whereas for the injection case in Figure 11c the positive peak stresses occur at the external corners (i.e., at $y = \pm 200$ m). This has potential consequences as will be discussed in the next section. Another, minor, difference is that the occurrence of localized reverse slip is not immediately clear from those earlier figures, because of the limitation of the Coulomb friction concept, although the possibility of reverse slip in displaced faults has been mentioned before; see Van den Bogert (2015) and Buijze et al. (2017, 2019).

The linear elastic assumptions underlying the analytical solutions in our paper are restrictive, and a full analysis of the development of aseismic and seismic slip along the fault would require nonlinear quasi-static and dynamic analyses, such as in Wassing et al. (2016), Van Wees et al. (2017), Buijze et al. (2019). However, our linear elastic analytical results do give an indication of some typical features of the development of injection- or production-induced seismic events in displaced faults as will be discussed below.

8. Insights

8.1. Onset of Slip

The occurrence of infinitely large elastic shear stresses at the corner points of the reservoir bordering the faults (at $y = \pm 100$ m and $y = \pm 200$ m in Figure 11) implies that even the smallest amount of injection or production will result in some amount of slip. As a consequence, in our model there does not exist a maximum injection level below which slip will be avoided when injecting in a faulted reservoir with finite fault throws. Similarly, there does not exist a "slip-free" minimum pressure for production from such a faulted reservoir. This is as opposed to earlier findings from numerical simulations of similar models in which spatial discretization limitations resulted in finite values of the elastic shear stresses; see, for example, Van den Bogert (2015) and Buijze et al. (2017). We note that in Figures 11b and 11c of our paper the shear stresses also erroneously display finite values at $y = \pm 100$ m and $y = \pm 200$ m, because of a finite resolution in the plotting algorithm; however, the singularities in the analytical elastic solution clearly indicate the presence of infinitely high elastic stresses at these points; see equation (16).

The infinite peaks in the shear stresses correspond to the perfectly sharp corners at the reservoir/fault interface in our reservoir model. In reality such sharp corners may not be present because the fault zone has a complex structure of breccia and gouge material. However, even though realistic shear stresses will not be infinitely large, they will still be sharply peaked and slip will already occur for small amounts of injection or production.

Earlier studies of production-induced slip in displaced faults indicate that slip will initially occur aseismically until a critical slip length has been achieved whereafter seismicity of an increasing magnitude will develop (Buijze et al., 2017, 2019; Van Wees et al., 2017). In particular, Buijze et al. (2017) demonstrate that the presence of peak shear stresses in a displaced fault leads to an earlier development of slip patches than in a fault without throw but that the resulting seismicity is typically lower because of a much longer period of aseismic slip preceeding it. In that sense the presence of infinitely large peaks in our analytical solu-

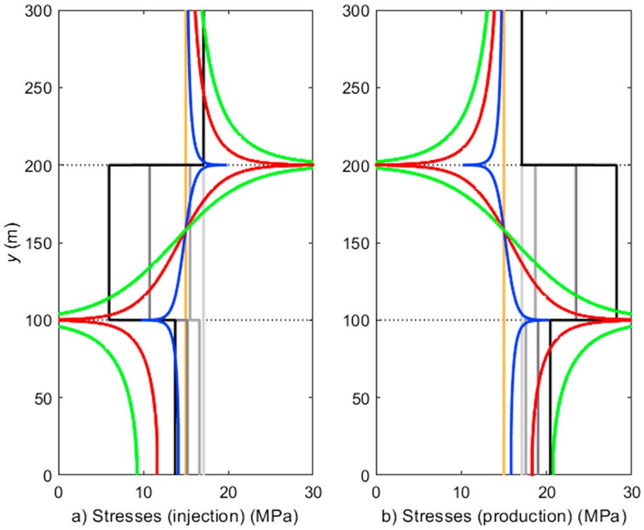

Figure 12. Shear stresses resulting from different incremental reservoir pressures p. (a) Injection; orange: $p = 0$ MPa, blue: $p = 5$ MPa, red: $p = 20$ MPa, green: $p = 35$ MPa. (b) Production; orange: $p = 0$ MPa, blue: $p = -5$ MPa, red: $p = -20$ MPa, green: $p = -35$ MPa. The gray and black lines in both figures indicate the right slip thresholds for increasing or decreasing pressures; light gray: $p = 0$ MPa, medium gray: $p = \pm5$ MPa, dark gray: $p = \pm20$ MPa, and black: $p = \pm35$ MPa. In both figures, slip is implied when a colored line is to the right of its corresponding threshold. Only the top half of the reservoir region ($0 \text{ m} < y \leq 300$ m) has been displayed.

tions, rather than the finite ones in earlier numerical studies, is a positive finding as it could imply a lower magnitude of induced seismic events.

8.2. Difference Between Injection and Production

Figure 12a depicts four shear stress distributions corresponding to the initial pressure and three increasing injection pressures. Note that, because of symmetry, only the top half of the fault has been displayed where $0 \text{ m} < y \leq 100$ m corresponds to "reservoir against reservoir," $100 \text{ m} < y \leq 200$ m to "reservoir against overburden," and $200 \text{ m} < y$ to "overburden against overburden." The figure also displays the right slip thresholds, corresponding to the four reservoir pressures, with gray and black lines. They display a shift because a change in pressure results in a change in the effective horizontal stress; see equations (22) and (23). The red and dark gray lines in Figure 12a, corresponding to $p = 20$ MPa, are identical to the red and gray lines in Figure 11c. Figure 12b depicts four similar shear stress distributions corresponding to the initial pressure and three decreasing production pressures where the largest pressure decrease ($p = -35$ MPa) implies full depletion of the reservoir (i.e., down to a reservoir pressure of 0 MPa).

A consequence of the different shear stress patterns for injection and production is that for injection a small increase in pressure results in an exceedance of the slip threshold at the external corners of the reservoir and the fault (i.e., at $y = \pm200$ m), whereas for the production case a small decrease in pressure results in slip at the internal corners (i.e., at $y = \pm100$ m). This implies that for the injection case some amount of slip occurs immediately in the overburden and underburden, whereas for production the slip remains inside the reservoir region, that is, inside the zones where either reservoir juxtaposes reservoir or where reservoir juxtaposes nonreservoir. If the fault is (near-)critically stressed, as in our example, the injection case will therefore likely result in seismic events with two growing slip regions, one above and one below the reservoir. Opposedly, the production case may also experience seismic (or aseismic) slip but with patches that mainly grow inward. Note that in the internal zones the slip thresholds increase in magnitude with increasing pressure drop which further reduces the severity of the seismicity in the production case. In reality the presence of gravity, and thus a pressure gradient, will break the symmetry around the x axis, and slightly different shear stress patters will emerge at the top and bottom parts of the reservoir. Moreover, differences in elastic properties between overburden and underburden may result in a preferential growth direction (Buijze et al., 2019). However, the essential difference in shear stress pattern between injection and production persists under these asymmetries.

As an aside, we note that the first observation of production-induced seismicity in the Groningen gas reservoir was only made after about half the reservoir was depleted and that it is generally concluded that this is a sign that the many faults in the reservoir are far from being critically stressed (Buijze et al., 2017; Van Wees et al., 2017). Although the absence of natural seismicity in the Groningen area strongly supports this conclusion, the possibility cannot be ruled out that the "internally directed" development of slip has played a role in the late development of seismicity in the Groningen field. The possibility that strongly negative shear stresses at the external corners act as barriers for the propagation of slip into the overburden and underburden has been mentioned before (Buijze et al., 2017, 2019; Van Wees et al., 2017; Zbinden et al., 2017), and our analytical results support these observations.

8.3. Slip Patch Growth

Another notable feature in the production situation is the partial exceedance of the (right) slip threshold by the "valley" in the shear stress near the middle of the reservoir (i.e., around $y = 0$ m). The valley in the blue line in Figure 12b is still almost completely to the left of the corresponding medium gray slip threshold and only the peaks at $y = \pm 100$ m result in small amounts of slip in two isolated patches that will each grow in both upward and downward directions with further decreasing pressure. The red line, corresponding to a 15 MPa lower pressure, is already partly crossing the dark gray slip threshold, while the valley in the green line, corresponding to another drop of 15 MPa, has completely crossed the black threshold and therefore indicates the occurrence of slip over the entire part of the fault where reservoir rock juxtaposes reservoir rock ($-100 < y < 100$ m). Once the shear stress at the "bottom of the valley" has passed the slip threshold, the growth of the two slip patches toward the middle of the reservoir ceases whereafter they will only grow in the direction of the overburden and underburden. For the fault in the production case in Example 1, the combined shear stress $\hat{\sigma}_{xy} = \sigma^0_{xy} + \sigma_{xy}$ follows from equations (16) and (25) as

$$\hat{\sigma}_{xy}(0, y) = \sigma^0_{xy} + \frac{C}{2} \ln \frac{(y-a)^2(y+a)^2}{(y-b)^2(y+b)^2}, \tag{26}$$

while the corresponding right slip threshold follows from equations (14) and (24) as

$$\sigma_{sl}(y) = -\mu_{\text{st}} \left[\sigma'^0_{xx} + \sigma'_{xx}(0, y) \right], \tag{27}$$

where (see also Figures 6 and 11a)

$$\sigma'_{xx}(0, y) = \begin{cases} 0 & \text{if} \quad y \leq -b \vee b \leq y \\ 2\pi C \left\{ \frac{1-\nu}{1-2\nu} - \frac{1}{2} \right. & \text{if} \quad -b < y \leq -a \vee a \leq y < b \\ 2\pi C \left\{ \frac{1-\nu}{1-2\nu} - 1 \right. & \text{if} \quad -a < y < a \end{cases} . \tag{28}$$

Intersections of the shear stress profile with the corresponding slip threshold can be obtained in closed form by solving for y from $\hat{\sigma}_{xy}(0, y) = \sigma_{sl}(y)$, with the aid of equations (26) to (28), resulting in values $y_{1,2,3,4}$ where $-b < y_1 < -a < y_2 < 0 < y_3 < a < y_4 < b$ as long as the slip patches have not merged and $y_2 < -b < y_1 < 0 < y_4 < b < y_3$ thereafter; see equations (63) and (64) in the supporting information. Figure 13 depicts the development of y_3 and y_4 with decreasing pressure, where y_3 and y_4 are the intersections of the upward and downward growing parts of the upper slip patch (i.e., the one emerging from $y = 100$ m). The figure shows an increasingly rapid decrease in the value of y_3 with decreasing pressure (i.e., an increasingly rapid growth of the "inner" slip patch length) when it approaches the value $y_3 = 0$, that is, just before it merges with the bottom slip patch that grows upward from $y = -100$ m. This effect has also been observed by Van den Bogert (2015). The red line in Figure 13 depicts the total slip half-length $L_{\text{sl}} = (y_4 - a) + (a - y_3) = y_4 - y_3$. The vertical dashed line indicates the pressure p_{mer} at which the patches will definitely have merged (according to elastic theory) which can also be determined in closed form; see equation (66) in the supporting information. For Example 1 shown in Figure 12b we find $p_{\text{mer}} = -30.8$ MPa, although the inelastic redistribution of stresses as a result of slip near the peaks will in reality result in an earlier merger.

The growth pattern of the fault slip with decreasing reservoir pressure is different from the development of the slip length in the injection case, where the two patches do not meet each other, at least not for the parameters chosen in Example 1; see Figure 12a. For different pressures, initial stresses, reservoir dimensions, and elastic properties, the merging of the two slip patches may occur earlier or may not occur at all. In particular, Example 1 concerns a case with a relatively high initial shear stress ($\sigma^0_{xy} = 15$ MPa, corresponding to an

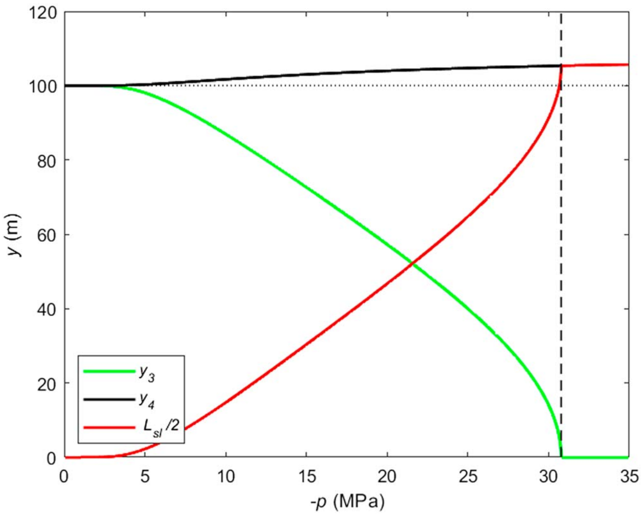

Figure 13. Intersections y_3 and y_4 of the shear stress profile with the slip threshold for the upper slip patch and total slip patch half-length $L_{sl}/2 = y_4 - y_3$ as a function of incremental pressure p during production. The figure illustrates the nonstationary growth in slip length (red curve) and the strong downward (green curve) and weak upward (black curve) growing tendency of the upper slip patch during production. (Note that this is an approximate result based on an elastic stress pattern without redistribution of stresses in the areas where the shear stresses exceed the slip boundary.)

SCU of 0.88). When repeating the example with only slightly lower values of σ_{xy}^0 (i.e., below $\sigma_{xy}^0 = 14.7$ MPa, corresponding to an SCU of 0.86), the merging was already absent even at full depletion. A small increase of the friction coefficient also leads to an absence of merging. At the other hand, inelastic stress redistribution and dynamic effects will influence these elastic (i.e., approximate) results and may lead to slip patch merging at milder depletion pressures.

8.4. Further Results

Various other relationships and insights can be obtained from the analytical expressions for a vertical fault provided in the supporting information such as, for example, an expression for the seismic moment, which happens to be identical to an earlier result obtained by Bourne and Oates (2017), an expression for the minimum pressure leading to slip patch merging during production, and another one for the excess shear force in the fault as a function of reservoir depletion; see section S4 of the supporting information. (Note that all these results are approximate because they are based on elastic stress patterns without redistribution of shear stresses in areas where these exceed the slip boundary.) An interesting observation is that integrals of the shear stresses, which are required to compute (excess) shear forces in the fault, are finite notwithstanding the singularities in the shear stresses. The closed-form nature of all these expressions makes it possible to obtain insights into their dependency on geometrical and stiffness parameters such as fault throw, reservoir height, shear modulus, and Poisson's ratio.

9. Expressions for an Inclined Fault

A similar application of inclusion theory as we used to obtain expressions for a vertical fault can be used to derive expression for the stresses in and around an inclined fault. Instead of considering two displaced rectangles, we then have to consider two trapezoids, each consisting of a triangle and a rectangle. The expressions become somewhat more cumbersome but can still be reproduced in compact form; see section S1 of the supporting information for a finite-width reservoir, section S2 for an infinitely wide reservoir, and section S3 for normal and shear stresses along the inclined fault plane in an infinite reservoir. The latter are given by

$$\begin{aligned} G_\perp = &-\frac{1}{2} \times \ln\left\{\frac{(y-a)^2(y+a)^2}{(y-b)^2(y+b)^2}\right\} \times \sin\theta\cos\theta \\ &-\frac{\pi}{2}\left[\operatorname{sgn}(y+b) - \operatorname{sgn}(y-a)\right] \times \sin^2\theta \\ &+\frac{\pi}{2}\left[\operatorname{sgn}(y+a) - \operatorname{sgn}(y-b)\right] \times (1+\cos^2\theta), \end{aligned} \tag{29}$$

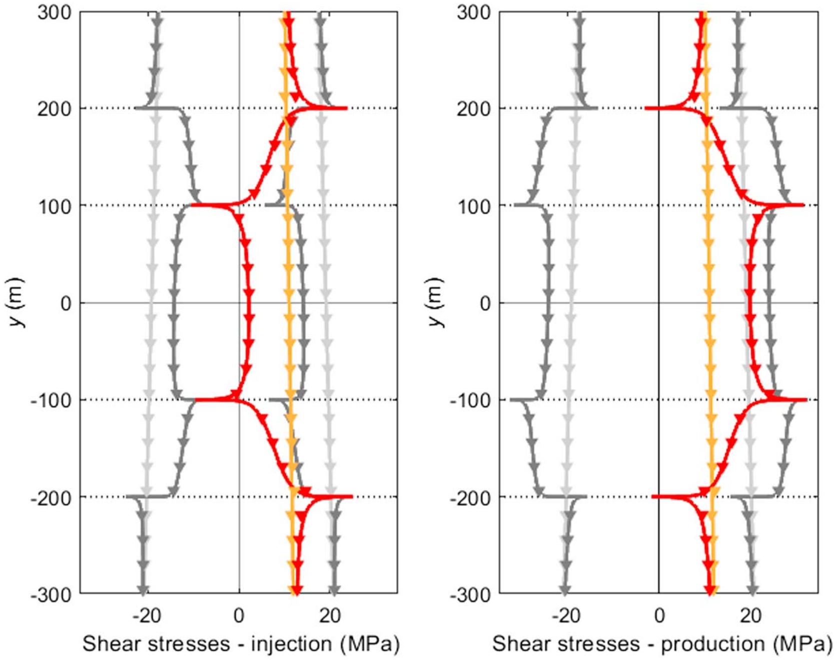

Figure 14. Shear stresses resulting from injection and production in a reservoir with an inclined normal fault ($\theta = \pi/3$; i.e., a 60° dip). Incremental reservoir pressure: $p = \pm 20$ MPa. Left: injection; right: production. Legend: orange: σ^0_{xy}; red: $\sigma^0_{xy} + \sigma_{xy}$. The gray lines indicate the corresponding slip thresholds; light gray: $\pm\mu_{\mathrm{st}}(\sigma'^0_{xx})$; dark gray: $\pm\mu_{\mathrm{st}}(\sigma'^0_{xx} + \sigma'_{xx})$. Shear values to the right of the corresponding right thresholds or to the left of the corresponding left thresholds will result in fault slip. The triangles represent numerical results, the solid lines the analytical ones.

$$
\begin{aligned}
G_{\parallel} = {} & \frac{1}{2} \times \ln\left\{ \frac{(y-a)^2(y+a)^2}{(y-b)^2(y+b)^2} \right\} \times \sin^2\theta \\
& - \frac{\pi}{2}\left[\operatorname{sgn}(y+a) - \operatorname{sgn}(y-a) - \operatorname{sgn}(y-b) + \operatorname{sgn}(y+b)\right] \times \sin\theta\cos\theta .
\end{aligned} \tag{30}
$$

Note that for $\theta = \frac{\pi}{2}$ these expressions for an inclined fault reduce to those for a vertical fault as given in equations (14) and (16). In analogy to the vertical results, $G_{\perp} - 2\pi\delta_{\Omega}$ and $G_{\parallel}$ represent scaled stresses that need to be multiplied with C to obtain their corresponding dimensional values.

Figure 14 depicts the shear stresses in an inclined displaced normal fault with a dip angle of 60°, resulting from injection ($p = 20$ MPa; left) or production ($p = -20$ MPa; right). The other relevant parameters are given in Table 2. As before, we consider an infinitely wide reservoir. The initial horizontal stress is now chosen to be a function of the vertical stress, according to a predefined ratio of effective horizontal to normal stresses $K' = 0.5$. The combined vertical and horizontal stresses can be resolved in normal and tangential (shear) components acting at the fault plane. It can be seen in Figures 14a and 14b that the initial shear stress (orange) is well below the corresponding slip threshold (light gray). Also, the shear stresses at 20 MPa overpressure (red curve; left) or 20 MPa depletion (red curve; right) remain below the slip threshold (dark gray) for nearly the entire fault. Only at the internal and external corners of the reservoir and the fault (i.e., at $y = \pm 100$ m and $y = \pm 200$ m), the shear stresses obtain infinitely high values, similar to what we observed for vertical faults; c.f. Figure 12.

To verify the analytical expressions, we computed the same stress patterns with a commercial geomechanics finite element code (Plaxis, 2016) where we calibrated the initial normal and shear stresses at the center of the fault (i.e. at $y = 0$). The initial and incremental stresses as computed numerically are depicted with triangles in Figure 14, and it can be seen that they generally correspond very well with the analytical results, except for the values near the singularities at $y = \pm 100$ m and $y = \pm 200$ m where the finite resolution of the numerical simulation does not allow for a detailed representation of the stress peaks.

Note that for the vertical fault in Figure 12 we disregarded gravity effects resulting in a symmetric stress field (with respect to the x axis) such that only positive y values needed to be displayed. Here we do con-

Table 2
Reservoir Properties and Fault Geometry for Example 2

Symbol	Property	Value	SI units
a	See Figure 1	100	m
b	See Figure 1	200	m
c	See Figure 1	∞	m
d	See Figure 1	∞	m
D_0	Depth at reservoir center ($y = 0$)	3,500	m
g	Acceleration of gravity	9.81	$\mathrm{m/s^2}$
G	Shear modulus	6,500	MPa
K'	Ratio of effective horizontal to vertical stress	0.5 or 1.2	—
p	Incremental reservoir pressure at reservoir center	±20	MPa
p^0	Initial reservoir pressure at reservoir center	35	MPa
α	Biot's coefficient	0.9	—
θ	Dip angle	$\pi/3$ or $5\pi/6$	rad
μ_{st}	Static friction coefficient	0.60	—
ν	Poisson's coefficient	0.15	—
ρ_f	Fluid density	1,020	$\mathrm{kg/m^3}$
ρ_s	Solid density	2,650	$\mathrm{kg/m^3}$
ϕ	Porosity	0.15	—

sider gravity, resulting in a slightly asymmetric stress pattern which therefore warrants displaying the entire reservoir height. The major qualitative difference between the two figures is in the shape of the slip thresholds for nonzero depletion: while in Figure 12 the thresholds have simple stepped shapes with finite values, in Figure 14 they are more curvy and contain infinite values because of the contribution of the logarithmic shear stress term G_{xy} to the normal stress $G_{\perp}$; see equation (29). (Recall that because of a finite resolution of the plotting algorithm, the infinite values corresponding to singularities at the internal and external corners are erroneously depicted as finite peaks.)

For a vertical fault, we concluded that the presence of infinitely large shear stresses at the internal and external reservoir/fault corners implies that even the smallest amount of injection or production will result in some amount of slip or other nonelastic deformation. It can be seen in Figure 14 that also for the inclined case there are always singularities, either at the internal or the external corners, where infinitely high shear stresses exceed slip thresholds with infinitely high values of opposite sign. Although infinitely high values do not occur in reality, because of nonelastic effects, this finding implies that also for inclined normal faults it is not meaningful to search for elastic solutions that correspond to slip-free maximum injection pressures or minimum production pressures.

As regards the other findings that we made for vertical faults, we conclude that qualitatively there is little difference between the response of vertical and inclined displaced normal faults. In particular, for vertical faults we observed an essential difference between injection and production in that injection causes an immediate growth of the slip patches into the overburden and underburden, whereas production results in an initial growth of the slip patches inside the reservoir; see the results of increasing and decreasing pressures in Figures 12a and 12b. Repeating the experiment for an inclined normal fault, we observed the same patterns.

Finally, we also investigated the stresses in inclined displaced reverse faults. Figure 15 depicts the situation for a case with $\theta = 5\pi/6$ (150°; that is, a 30° dipping reverse fault) and $K' = 1.2$, both for injection and production. It can be seen that qualitatively the same results are obtained as for normal faults. The major difference is that because of the relatively large horizontal stress, which is a necessity to cause reverse (thrust) faulting, the slip thresholds have much higher (absolute) magnitudes than in the normal faulting example in Figure 14 such that the SCU is, on average, much smaller.

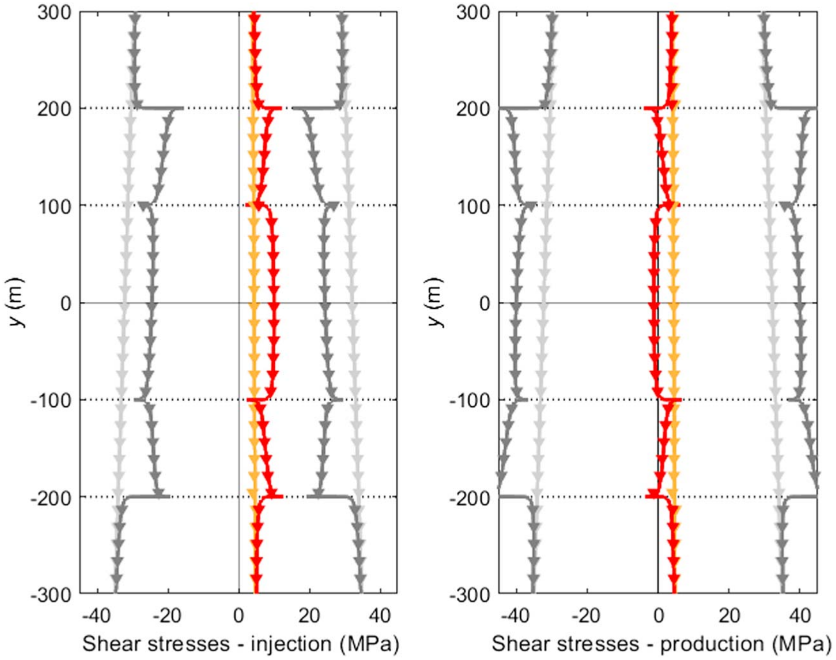

Figure 15. Shear stresses resulting from injection and production in a reservoir with an inclined reversed fault ($\theta = 5\pi/6$; i.e., a 30° dip). Key as in Figure 14.

10. Conclusions

We considered the elastic displacements, strains, and stresses resulting from injection into or production from finite-width or infinite-width reservoirs containing a displaced fault. As a first step we derived closed-form expressions for a 2-D homogeneous infinite-width reservoir with a vertical fault. We applied those to an example with reservoir properties mostly of the same order of magnitude as those of the Groningen natural gas reservoir and obtained the following insights:

- We confirmed and sometimes sharpened several findings from earlier numerical studies. This concerns in particular the following results which were described or mentioned before in some form by Van den Bogert (2015), Buijze et al. (2017), Van Wees et al. (2017), Zbinden et al. (2017), and recently, Buijze et al. (2019).
- The elastic stress patterns for incremental horizontal, vertical, and shear stresses are independent of the magnitude of the incremental pressure p and only depend on the values of the geometric reservoir parameters. The pressure acts as a linear multiplier for the magnitude of the scale. In reality, the occurrence of fault slip will result in a nonelastic redistribution of stresses such that an increasing or decreasing p does influence the stress patterns.
- Production from a reservoir with a displaced fault produces a peaked shear stress profile with large positive (slip-provoking) shear stresses at the internal corners of the reservoir-fault interface and the presence of strongly negative shear stresses at the external corners which act as barriers for the propagation of slip into the overburden and underburden in case of production-induced seismicity.
- At high initial positive shear stress levels, corresponding to a (near-)critically stressed fault, the two slip patches in the production case grow mainly inward into the reservoir at an exceedingly high rate with decreasing reservoir pressure until they merge. The effect is strongly sensitive to initial shear stress, and friction coefficient values and merging may or may not occur for production. For the injection case merging is unlikely to occur anyway. Aseismic or seismic slip leading to readjustment of the fault stress may accelerate the merging.

In addition, we made the following observations:

- The development of infinitely large elastic shear stresses in a displaced fault, at the sharp internal and external reservoir/fault corners, implies that even the smallest amount of injection or production will result in some amount of slip or other nonelastic deformation. As a consequence there does not exist a maximum injection level below which slip will be avoided when injecting in a faulted reservoir with sharp reservoir/fault corners. Similarly, there does not exist a slip-free minimum pressure for production from such an idealized faulted reservoir. This conclusion may not strictly hold for more elaborate reservoir models that contain realistic details of the reservoir/fault corner regions. However, also in those cases the occurrence of slip for small amounts of injection or production is very likely.

- There is a marked difference between the shear stress patterns resulting from injection and production in a reservoir with a displaced fault. In both situations two slip patches emerge. However, for the injection case an increase in pressure results in an exceedance of the slip threshold at the external corners of the reservoir and the fault, whereas during production a decrease in pressure results in slip at the internal corners. This implies that at the start of injection some amount of slip occurs immediately in the overburden and underburden, whereas during production the slip may remain inside the reservoir region.
- Various closed-form expressions can be derived that describe specific aspects of induced seismicity in reservoirs with a displaced fault. These include an expression for the seismic moment, earlier found by Bourne and Oates (2017), the excess (nonelastic) shear force and the length of slip patches as a function of incremental pressure, and the pressure at which slip patches merge according to elastic theory.

Next, we derived closed-form expressions for an inclined fault and concluded that the findings for displaced vertical faults as listed above also apply to displaced inclined (normal or reverse) faults.

We note that these conclusions are based on an analytical elastic model of a displaced fault that does not take into account aseismic or seismic stress redistribution after the onset of slip. More elaborate numerical studies that were performed earlier and that did take into account inelastic and dynamic effects displayed typically similar stress patterns, and we therefore hypothesize that our conclusions will also hold under more realistic conditions. Other assumptions include the simplified 2-D shape of the reservoir and the use of an infinite space rather than a half-space; absence of gravity, multiphase, and pressure transient effects; a perfectly straight and infinitely thin fault that does not transmit pressure beyond the reservoir boundaries; and the use of uniform elastic properties for the reservoir and its surroundings. Clearly, an analytical model with so many simplifications is not intended to provide quantitative results with predictive value for real reservoirs, for which field observations, laboratory experiments, and numerical simulations will be essential. However, we consider the insights from our closed-form solutions to be of relevance for the interpretation of such experimental and numerical work and hope that they will be a source of inspiration for continued research into injection- and production-induced seismicity.

Acknowledgments

We acknowledge the support of Ronald Brinkgreve and Irene Platteeuw regarding the use of Plaxis 2-D for the numerical calculations. The Matlab files used to produce most of the figures in this paper as well as the input files used for the Plaxis 2-D verification are available from the 4TU data repository. Matlab files (http://doi.org/10.4121/uuid:d8ca79ae-17fb-4c60-b86b-08c495b2722f) and Plaxis files (http://doi.org/10.4121/uuid:1b121d28-39f4-40ff-b5e8-c3ae5aa90767).

References

Bhargava, R., & Kapoor, O. (1966). Two-dimensional rectangular inclusion. *Proceedings of the National Academy of Sciences, India Part A*, *32*(1), 46–55.

Biot, M. A. (1941). General theory of three-dimensional consolidation. *Journal of Applied Physics*, *12*, 155–164. https//doi.org/10.1063/1.1712886

Bourne, S. J., & Oates, S. J. (2017). Extreme threshold failures within a heterogeneous elastic thin sheet and the spatial-temporal development of induced seismicity within the Groningen gas field. *Journal of Geophysical Research: Solid Earth*, *122*, 10,299–10,320. https//doi.org/10.1002/2017JB014356

Buijze, L., Van den Bogert, P., Wassing, B., & Orlic, B. (2019). Nucleation and arrest of dynamic rupture induced by reservoir depletion. *Journal of Geophysical Research: Solid Earth*, *124*, 3620–3645. https//doi.org/10.1029/2018JB016941

Buijze, L., Van den Bogert, P., Wassing, B., Orlic, B., & Ten Veen, J. (2017). Fault reactivation mechanisms and dynamic rupture modelling of production-induced seismic events in a Rotliegend gas reservoir. *Netherlands Journal of Geosciences*, *96*(5), S131—S148. https//doi.org/10.1017/njg.2017.27

Cappa, F., & Rutqvist, J. (2011). Impact of CO_2 geological sequestration on the nucleation of earthquakes. *Geophysical Research Letters*, *38*, L17313. https//doi.org/10.1029/2011GL048487

Cheng, A. H.-D. (2016). *Poroelasticity*. Switzerland: Springer.

Dougall, J. (1897). A general method of solving the equations of elasticity. *Proceedings of the Edinburgh Mathematical Society*, *16*(1), 82–98. https//doi.org/10.1017/S0013091500032430

Eshelby, J. D. (1957). The determination of the elastic field of an ellipsoidal inclusion and related problems. *Proceedings of the Royal Society of London. Series A*, *241*, 376–396. https//doi.org/10.1098/rspa.1957.0133

Gambolati, G. (1972). A three-dimensional model to compute land subsidence. *Hydrological Sciences Bulletin*, *17*(2), 219–226. https//doi.org/10.1080/02626667209493823

Geertsma, J. (1966). Problems of rock mechanics in petroleum production engineering. In *Proc.* 1st *ISRM Congress*. (25 Sept.-1 Oct., Lisbon, Portugal) (pp. 585–594).

Geertsma, J. (1973). A basic theory of subsidence due to reservoir compaction: The homogeneous case. *Verhandelingen Koninklijk Nederlandsch Geologisch Mijnbowkundig Genootschap*, *2S*, 43–61.

Goodier, J. (1937). On the integration of the thermo-elastic equations. *The London, Edinburgh, and Dublin Philosophical Magazine and Journal of Science*, *23*(157), 1017–1032. https//doi.org/10.1080/14786443708561872

Haug, C., Nüchter, J.-A., & Henk, A. (2018). Assessment of geological factors potentially affecting production-induced seismicity in North German gas fields. *Geomechanics for Energy and the Environment*, *16*, 15–31. https//doi.org/10.1016/j.gete.2018.04.002

Huynen, A., & Detournay, E. (2014). A remark on the poroelastic center of dilation. *Journal of Elasticity*, *116*, 189–206. https//doi.org/10.1007/s10659-013-9461-2

Lele, S., Hsu, S.-Y., Garzon, J., DeDontney, N., Searles, K., Gist, G., et al. (2016). Geomechanical modeling to evaluate production-induced seismicity at Groningen field. In *Proc. Abu Dhabi International Petroleum Exhibition and Conference* (pp. 1–18). https//doi.org/10.2118/183554-MS. (7-10 Nov., Abu Dhabi, UAE).

Love, A. (1927). *A treatise on the mathematical theory of elasticity* (4th ed.). Cambridge. Reprinted in 1944 by Dover, New York: Cambridge University Press.

Marck, J., Savitski, A. A., & Detournay, E. (2015). Line source in a poroelastic layer bounded by an elastic space. *International Journal for Numerical and Analytical Methods in Geomechanics*, *39*, 1484–1505. https//doi.org/10.1002/nag.2405

Mulders, F. (2003). Modelling of stress development and fault slip in and around a producing gas reservoir (Doctoral dissertation), Delft University of Technology. http://resolver.tudelft.nl/uuid:be742135-10d7-4d69-bdee-f808b5926065

Mura, T. (1987). *Micromechanics of defects in solids* (2nd ed.). Dordrecht: Martinus Nijhoff Publishers.

NAM (2016). Winningsplan> Groningen gasveld (Tech. Rep.). The Netherlands: Nederlandse Aardolie Maatschappij. http://www.nam.nl/gas-en-oliewinning/groningen-gasveld/winningsplan-groningen-gasveld.html

Nagelhout, A., & Roest, J. (1997). Investigating fault slip in a model of an underground gas storage facility. *International Journal of Rock Mechanics and Mining Sciences*, *34*(3,4), 212.e1–212.e14. https//doi.org/10.1016/S1365-1609(97)00051-8

Orlic, B., & Wassing, B. (2013). A study of stress change and fault slip in producing gas reservoirs overlain by elastic and viscoelastic caprocks. *Rock Mechanics and Rock Engineering*, *46*, 421–435. https//doi.org/10.1007/s00603-012-0347-6

Orlic, B., Wassing, B., & Geel, C. (2013). Field scale geomechanical modeling for prediction of fault stability during underground gas storage operations in a depleted gas field in the Netherlands. In *47th US Rock Mechanics / Geomechanics Symposium*. (Paper ARMA-13-300. 23-26 June, San Francisco, USA) (11 pp).

Plaxis (2016). https://www.plaxis.com/product/plaxis-2d/

Roest, J., & Kuilman, W. (1994). Geomechanical analysis of small earthquakes at the Eleveld gas reservoir. In *SPE-ISRM Rock Mechanics in Petroleum Engineering Conference* (pp. 573–580). https//doi.org/10.2118/28097-MS. (Paper SPE 28097.29-31 Aug., Delft, The Netherlands).

Rudnicki, J. W. (1999). Alteration of regional stress by reservoirs and other inhomogeneities: Stabilizing or destabilizing? In *9th ISRM Congress*. (25-28 Aug., Paris, France) (pp. 1629–1637).

Rudnicki, J. (2002). Elsheby transformations, pore pressure and fluid mass changes, and subsidence. In *Poromechanics II, 2nd Biot Conf. Poromech.* (Aug. 26-28 Grenoble, France) (pp. 307–312).

Rutqvist, J., Rinaldi, A. P., Cappa, F., Jeanne, P., Mazzoldi, A., Urpi, L., et al. (2016). Fault activation and induced seismicity in geological carbon storage—Lessons learned from recent modeling studies. *Journal of Rock Mechanics and Geotechnical Engineering*, *8*(6), 789–804. https//doi.org/10.1016/j.jrmge.2016.09.001

Segall, P. (1985). Stress and subsidence resulting from subsurface fluid withdrawal in the epicentral region of the 1983 Coalinga earthquake. *Journal of Geophysical Research*, *90*(B8), 6801–6816. https//doi.org/10.1029/JB090iB08p06801

Segall, P. (1989). Earthquakes triggered by fluid extraction. *Geology*, *17*(10), 942–946. https//doi.org/10.1130/0091-7613(1989)017<0942:ETBFE>2.3.CO;2

Segall, P. (1992). Induced stresses due to fluid extraction from axisymmetric reservoirs. *Pure and Applied Geophysics*, *139*(3-4), 535–560. https//doi.org/10.1007/BF00879950

Segall, P., & Fitzgerald, S. (1998). A note on induced stress changes in hydrocarbon reservoirs and geothermal reservoirs. *Tectonophysics*, *289*, 117–128. https//doi.org/10.1016/S0040-1951(97)00311-9

Segall, P., Grasso, J., & Mossop, A. (1994). Poroelastic stressing and induced seismicity near the Lacq gas field, southwestern France. *Journal of Geophysical Research*, *99*(B8), 15,423–15,438. https//doi.org/10.1029/94JB00989

Soltanzadeh, H., & Hawkes, C. D. (2008). Semi-analytical models for stress change and fault reactivation induced by reservoir production and injection. *Journal of Petroleum Science and Engineering*, *60*, 71–85. https//doi.org/10.1016/j.petrol.2007.05.006

Soltanzadeh, H., & Hawkes, C. D. (2009). Assessing fault reactivation tendency within and surrounding porous reservoirs during fluid production or injection. *International Journal of Rock Mechanics and Mining Sciences*, *46*, 1–7. https//doi.org/10.1016/j.ijrmms.2008.03.008

Thibault, C., Wassing, B., Ter Heege, J., & Buijze, L. (2018). How earthquakes are induced. *Science*, *360*(6389), 598–600. https//doi.org/10.1126/science.aat2776

Van Wees, J. D., Buijze, L., Van Thienen-Visser, K., Nepveu, M., Wassing, B. B. T., Orlic, B., & Fokker, P. A. (2014). Geomechanics response and induced seismicity during gas field production in the Netherlands. *Geothermics*, *52*, 206–219. https//doi.org/10.1016/j.geothermics.2014.05.004

Van Wees, J., Fokker, P., Van Thienen-Visser, K., Wassing, B., Osinga, S., Orlic, B., et al. (2017). Geomechanical models for induced seismicity in the Netherlands: Inferences from simplified analytical, finite element and rupture model approaches. *Netherlands Journal of Geosciences*, *96*(5), S183—S202. https://doi.org/10.1017/njg.2017.38

Van Wees, J., Osinga, S., Van Thienen-Visser, K., & Fokker, P. (2018). Reservoir creep and induced seismicity: Inferences from geomechanical modeling of gas production in the Groningen field. *Geophysical Journal International*, *212*(3), 1487–1497. https//doi.org/10.1093/gji/ggx452

Van den Bogert, P. (2015). Impact of various modelling c slip response using 2-dimensional finite-element modelling (*Restricted report No. SR.15.11455*). The Netherlands: NAM. https://nam-feitenencijfers.data-app.nl/download/rapport/604ef59b-5ac5-4770-93b1-e501c87da3a9?open=true

Verruijt, A. (2016). Theory and problems of poroelasticity. geo.verruijt.net.

Walsh, J. (2002). Subsidence above a planar reservoir. *Journal of Geophysical Research*, *107*(B9), 2202. https//doi.org/10.1029/2001JB000606

Wang, H. (2000). *Theory of linear poroelasticity with applications to geomechanics and hydrogeology*. Princeton: Princeton University Press.

Wassing, B., Buijze, L., & Orlic, B. (2016). Modelling of fault reactivation and fault slip in producing gas fields using a slip-weakening friction law. In *50th Rock Mechanics Symposium*. (Paper ARMA 16-658. 26-29 June, Houston, USA) (11 pp).

Zbinden, D., Pio Renaldi, A., Urpi, L., & Wiemer, S. (2017). On the physics-based processes behind production-induced seismicity in natural gas fields. *Journal of Geophysical Research: Solid Earth*, *122*, 3792–3812. https//doi.org/10.1002/2017JB014003